3D Geometric Modelling of Discontinuous Fibre Composites Using a Force Directed Algorithm

L.T. Harper*, C. C. Qian, R. Luchoo, N.A. Warrior

Division of Materials, Mechanics and Structures, Faculty of Engineering,
University of Nottingham, NG7 2RD, United Kingdom
* Corresponding author (lee.harper@nottingham.ac.uk)

Abstract

A geometrical modelling scheme is presented to produce representative architectures for discontinuous fibre composites, enabling downstream modelling of mechanical properties. The model generates realistic random fibre architectures containing high filament count bundles (>3k) and high (~50%) fibre volume fractions. Fibre bundles are modelled as thin shells using a multi-dimension modelling strategy, in which fibre bundles are distributed and compacted to simulate pressure being applied from a matched mould tool. FE simulations are performed to benchmark the in-plane mechanical properties obtained from the numerical model against experimental data, with a detailed study presented to evaluate the tensile properties at various fibre volume fractions and specimen thicknesses. Tensile modulus predictions are in close agreement (less than 5% error) with experimental data at volume fractions below 45%. Ultimate tensile strength predictions are within 4.2% of the experimental data at volume fractions between 40%-55%. This is a significant improvement over existing 2D modelling approaches, as the current model offers increased levels of fidelity, capturing dominant failure mechanisms and the influence of out-of-plane fibres.

Keywords: Discontinuous composite, finite element analysis, force directed algorithm,

1 Introduction

Discontinuous fibre composites (DFCs) offer great potential for high volume applications (50,000ppa +) because of their short cycle times and low processing costs compared with textile-based composites. Carbon fibre Sheet Moulding Compounds (SMCs) offer some of the highest tensile properties for DFCs commercially available, with stiffness and ultimate strength values reported to be up to 45GPa and 300MPa respectively [1-3]. The filaments in carbon fibre SMCs are typically arranged randomly in bundle form (typically 24,000 filaments per bundle), limiting the global fibre volume fractions to around 55%. The initial fibre charge covers a large area of the mould tool (up to 90%), so material flow under pressure is minimal, which ensures that the fibres remain in bundle form whilst facilitating long fibre lengths (up to 50mm). DFCs are versatile and their mechanical properties span a wide range [4-6], but it is difficult to control the high levels of material variability compared with continuous fibre composites. Due to this, a large number of test specimens is required to achieve suitable confidence in experimental data [7, 8]. This is both time consuming and costly, particularly as mechanical properties can also be influenced by size and scale [9-14] due to the random heterogeneous nature of the material. This prevents the standard “building block approach” [15] from being used, where coupon testing provides data for design, which is then validated by a scale-up towards a complete part using sub-components and structural elements.

Finite Element Analysis (FEA) can be used to predict the mechanical properties of DFCs [16-18] and to understand the source of variability, but accuracy is limited due to the quality of the fibre architectures generated for the meso-scale Representative Volume Element (RVE) [19]. Existing numerical models for generating RVEs can be classified into three main groups [20]; soft, hard and sedimentation models and each has its limitations. Soft models allow overlapping fibre bundles and are therefore unrealistic, as no restriction on fibre volume fraction is imposed. Allowing bundle-bundle penetration also creates incorrect load transfer paths at bundle cross-overs. Hard models prevent bundle-bundle penetration, but fibre volume fractions are limited due to fibre jamming, which is commonly experienced when the pockets of free space are too small to accept additional inclusions. Sedimentation algorithms are hard systems with restrictions on the orientation distribution [21]. Although the restriction on the ceiling volume fraction is reduced, sedimentation algorithms are computationally expensive [20] and creating meshes for hard or sedimentation models can be problematic, due to the small separation distances between bundles.

RVE size is linked to the fibre length and tow size [7] and can be several orders of magnitude larger than the scale of the reinforcement. Computation time is therefore one of the primary concerns associated with meso-scale FEA models for DFC materials. 2D models are the most computationally inexpensive option, using 1D linear beam elements to represent fibre bundles randomly distributed in 2D space [7, 22-26]. However, this approach overlooks fibre crimping and allows bundle-bundle penetration, as all bundles are deposited on the same plane,

reducing accuracy. 2D models also tend to be over-stiff, as intersecting bundles are rigidly bonded at the intersection point [25], which increases as the RVE thickness increases.

Three dimensional hard models have previously been developed [27, 28] using continuum elements to represent the fibre bundles. Bundles were assumed to be straight with circular cross section, limiting the maximum achievable volume fraction to ~13.5%. Further developments [29] enabled fibre curvature and elliptical cross sections, increasing the volume fraction of the cell to 35%. Pan et al. [29] used Halpin-Tsai predictions to benchmark the FEA stiffness results, indicating relative errors of 5.8% and 12% for the tensile and shear moduli respectively. Ignoring fibre curvature can artificially increase the predicted UTS values by up to 18% [30, 31].

A pre-processing scheme is presented in this paper to produce highly representative DFC architectures. These architectures can be used to create finite element meshes for determining mechanical properties at the mesoscale, providing an alternative to expensive experimental testing for producing coupon data. The model aims to characterise random fibre materials containing large filament count bundles (>3K) and high fibre volume fractions (~50%). Fibre bundles are modelled as shells using a so-called mixed-dimensional modelling strategy [32], which enables the bundles to be redistributed and compressed to simulate pressure being applied from a matched mould tool. A force-directed algorithm is adopted to simulate the through-thickness compliance of the fibre bundles, in order to achieve realistic local fibre distributions. RVE quality is assessed with respect to geometric detail, the quantity

of bundle-bundle intersections and convergence times. FE simulations are performed to predict the tensile properties for the fibre architectures produced by the numerical model, which are validated against experimental data.

2 Geometric modelling scheme

The geometric modelling scheme consists of three parts: A deposition algorithm to determine initial bundle locations and orientations; an intersection-elevation algorithm to detect and avoid bundle-bundle intersections, and a spline interpolation algorithm to produce smooth curved fibre bundles. This approach provides intimately packed fibre bundles and increases the fibre volume fraction limits associated with existing models. A flowchart of the geometric modelling scheme is presented in Figure 1, which is explained in more detail in the following sections.

2.1 Deposition algorithm

The bundle deposition algorithm is based on the 2D algorithm developed in [25]. Rectangular fibre bundles of user-specified length and tow size are generated, where bundle widths for each tow size (K) have been derived experimentally [15] (see Table 1). Random numbers are generated within specified bounds (the defined RVE) for the x, y and z coordinates of the geometric centre of each fibre bundle. A fourth random number is generated for the in-plane fibre orientation about the same centre. Each bundle is deposited sequentially within the RVE and a Liang-Barsky algorithm [33, 34] is employed to crop the bundle if it crosses the

boundary. This method ensures that edge effects are not introduced within the RVE, ensuring the region of interest will exhibit representative material properties. A hard-walled boundary approach has not been used as this can result in preferential fibre alignment along the cell walls [35], as the experimental coupons used for validation have been cut from a larger plaque rather than moulded net-shape. Fibre bundles are continuously deposited over the region of interest until the target fibre volume fraction has been achieved.

2.2 Intersection-elevation algorithm

The intersection-elevation algorithm uses a force-directed approach to prevent bundle intersections. It should be noted that this does not represent the true interaction mechanisms between the fibre bundles, it merely aims to minimise/eliminate fibre-fibre intersections by introducing fibre curvature and crimp. Fibre deformation mechanism such as tow fragmentation and spreading, which commonly occur in compression moulding processes, are not considered in this paper.

An initial nodal network [36] is created (shown in Figure 2) and an attraction-repulsion mechanism is used to define the spatial distribution [20, 37], in order to separate neighbouring fibre bundles. Each node is charged with charge Q, repelling any neighbouring nodes in close proximity using Coulomb's inverse square law:

$$F_{REPULSION} = k_{REPULSION} Q^2/r^2 \quad \textbf{Equation 1}$$

where $k_{REPULSION}$ is the Coulomb force constant, and r is the separation distance between two nodes.

The distribution of nodes is controlled by connecting springs, causing attraction forces under Hooke's law. For springs with axial stiffness, k_{AX}

$$F_{ATTRACTION} = -k_{AX}\delta L \quad \textbf{Equation 2}$$

where δL is the change in natural spring length. For springs with rotational (torsion) stiffness, k_{RT}

$$F_{TORSION} = -k_{RT}(\pi - \Theta) \quad \textbf{Equation 3}$$

where Θ is the twisting angle of the spring in radians and π is the natural spring angle.

Two types of node exist; parent nodes and sister nodes. Sister nodes are distributed uniformly around the perimeter of each bundle, shown as spheres in Figure 2. Neighbouring sister nodes belonging to the same bundle are connected by sister springs with axial stiffness $k_{SISTER\text{-}AX}$ and rotational stiffness $k_{SISTER\text{-}RT}$. The axial stiffness provides a force to maintain the original bundle dimensions, and the rotational stiffness controls the fibre curvature and crimp. This is appropriate for DFCs that experience very little in-mould fibre flow, such as those created by the directed fibre preforming process [38].

Each sister node is connected to a pair of parent nodes by parent springs (with axial stiffness $k_{PARENT\text{-}AX}$ and rotational stiffness $k_{PARENT\text{-}RT}$), in order to control the Z movement of each bundle. Parent nodes are located on the top and bottom surfaces of the RVE and are shown as cubes in Figure 2. The natural length of the parent springs has been chosen to be equal to the thickness of an impregnated bundle to prevent unrealistic distances between neighbouring fibres and cell surfaces. The thickness of the bundle is dependent on the filament count, as presented in Table 1. Consequently, the RVE shown in Figure 2 is not in equilibrium.

As the number of bundles deposited within the RVE increases, the likelihood of a bundle-bundle intersection increases. Intersections are handled by adjusting the nodal network around the intersection point and two scenarios are considered in this work: edge-edge intersection (Figure 3) and edge-surface intersection (Figure 4). Edge-edge intersection can be detected when the edge of Bundle A penetrates through the edge of Bundle B (Figure 3) and can happen either at the beginning of fibre deposition process, when fibre bundles are initially planar, or after the intersection-elevation algorithm has been evoked for neighbouring bundles. Here an additional pair of sister nodes is created on each bundle, one at the intersection location and the other on the opposite edge. Each pair of additional sister nodes is connected to new sister springs with axial stiffness to prevent lateral spreading of the bundle. Additional nodes on Bundle A and Bundle B are then moved apart under the repulsion force according to Equation 1, to remove edge-edge intersection.

Edge-surface intersection can be detected when the edge of fibre Bundle A penetrates through the surface of fibre Bundle B without touching the edge of Bundle B (Figure 4). Edge-surface intersections can only occur after the intersection-elevation algorithm has been evoked, when fibre bundles are non-planar. Edge-surface intersections are eliminated by projecting some of the parent nodes from Bundle A onto the surface of Bundle B, as shown in Figure 4. Consequently, the upward forces in the parent springs above Bundle A exceed the downward forces in the parent springs below Bundle A, resulting in Bundle A moving away from Bundle B. During interaction-elevation operation, the net force exerted on each node is calculated using Equations 1 to 3. The magnitude of the net force is multiplied by a dimensionless damping factor c $(0 < c < 1)$, in order to control the stability of the intersection-elevation process. A sensitivity analysis has been performed to determine a value for c and results indicate that the minimum acceptable value is 3×10^{-6}.

2.3 Spline interpolation algorithm

Small adjustments to the sister nodes are performed to smooth fibre undulations and to provide realistic crimp angles. This is achieved by interpolating a Catmull-Rom spline through all sister nodes on the fibre boundary, where spline quality is controlled by the distance between nodes. This type of polynomial spline provides a continuously varying tangent (no discontinuities) along the tow path and is computationally inexpensive to define and implement. Additional dummy sister nodes are added at each bundle end to provide the minimum number of points required for spline interpolation for bundles that have been

cropped at the RVE boundary [39]. The implementation of the spline interpolation algorithm is discussed in detail in [31]. It should be noted that spline interpolation can introduce further edge-edge and edge-surface intersections, which increase in numbers as the curvature of the edge increases. The resulting nodal network does not always violate the intersection-elevation criteria and consequently these defects only become apparent after meshing. Small intersections can therefore appear after spline interpolation, particularly for higher volume fraction RVEs where fibre curvatures are generally greater. Intersections resulting from spline interpolation do not prevent the part from being meshed or simulations being performed for FE mechanical property prediction.

2.4 Stopping criteria

An iterative approach is adopted in this model to optimise fibre bundle distribution. The net force (after damping) applied on each node is recalculated in each iteration and nodes are displaced. The damping factor *c* is gradually increased from the minimum value ($3x10^{-6}$) during the iterative process and the increment is determined by a convergence check performed every 100 iterations. The convergence check evaluates the total number of bundle-bundle intersections (summation of edge-edge intersections and edge-surface intersections) and the total strain energy of the spring system. If either the total number of bundle-bundle intersections or the total energy has been reduced, no increment in *c* is applied. Alternatively, *c* is increased by 20% if neither has reduced and the total number of intersections is non-zero, or by 50% if the total number of intersections is zero. The algorithm stops when *c* equals unity.

A sensitivity study has been performed to determine the optimum spring and node-charge constants. The quality of the chosen parameters is assessed by the percentage number of bundle-bundle intersections once the system energy has converged, where the percentage is calculated as the ratio of the number of intersecting points to the total number of nodes within the fibre network. RVE architectures for a 50% Vf with 36mm long, 12K fibre bundles have been adopted for the sensitivity analysis and the optimum spring and node-charge constants are listed in Table 2.

A variety of architectures with different bundle sizes have been generated using the variables in Table 2 and are presented in Figure 5. Realistic RVE architectures are created, which are physically similar to real fibre architectures (Figure 6) produced using a laboratory scale DFC installation [40]. Bundles are evenly distributed through the thickness of the RVE, with experimentally realistic fibre crimp. Results suggest that the model can reliably generate intersection-free fibre architectures for small bundle sizes (3K) at fibre volume fractions of ~50%, and for large bundle sizes (12K) at fibre volume fractions of ~40%. For fibre content higher than these limits, excessive fibre distortion and/or bundle to bundle penetration has been seen to occur. Examples of bundle penetration are shown in Figure 5b and Figure 5d for unrealistic fibre architectures of 60% fibre volume fraction. It should be noted however, that the program will continue running with the presence of these bundle to bundle penetrations.

Figure 7 shows the CPU time and required number of iterations for convergence for a 38x38x3mm cell consisting of 12K, 36mm fibre bundles at a range of fibre volume fractions

(using an Intel Core i3 processor with 8GB of RAM). Convergence times were over 4 hours for a typical realisation with a 60% Vf, 38×38×3mm RVE. This value increases dramatically (over 24 hours) for larger RVEs (140×140×3mm). The required number of iterations for convergence is shown to be directly proportional to the number of charged nodes in the RVE nodal network. A quadratic relationship is observed between solution times and number of nodes.

3 FEA modelling for mechanical properties prediction

3.1 Mesh generation

Each fibre bundle is meshed independently with a custom Delaunay algorithm, to accommodate the irregular polygon surfaces resulting from the cropping algorithm. Firstly, the RVE cell boundary is offset internally by a distance that is equivalent to 10% of the seed size used to mesh the fibre bundles. Mesh seeds falling between the two cell boundaries are removed. Secondly, a minimum facet angle of 5° is specified. An additional seed is placed at the element's circumcentre if the facet angle is less than the threshold value [41] and the fibre is re-meshed. Figure 8 shows an example of a meshed model. The seed size for the fibre elements was approximately 10% of the measured bundle width and quadratic ABAQUS STRI65 triangular shell elements were chosen to avoid potential hour-glassing effects.

The matrix material is modelled using a regular array of linear 8-noded brick elements (ABAQUS type C3D8). Shell elements representing the fibre bundles are tied to the continuum elements using the *EMBEDDED ELEMENT technique, where the translational displacements

of the embedded shell element nodes (fibre) are determined by the translational displacements of the host continuum element nodes (matrix). Using embedded elements eliminates the need for a complex meshing algorithm to pair coincident nodes on the fibres/resin interface. The benefit of this approach has been demonstrated in previous work [25] using beam elements to represent fibre bundles and 2D continuum elements to represent matrix. The local stress distribution was shown to be the same as using tie constraints to join the two unstructured meshes at the fibre/resin interface. However, it should be noted that using the embedded element technique may compromise the accuracy of the model in terms of failure prediction, as the fibre-matrix interfacial properties cannot be considered, as debonding is prohibited.

A simple RVE containing two fibre bundles, subjected to tensile loading conditions, has been created (Figure 9) to demonstrate the suitability of the proposed embedded element approach for the 3D architectures studied here. Two fibre bundles are orientated at 0˚ and 45˚ to the loading direction and the principal stress (S11) and interfacial shear stress (S12) distributions are plotted along the centreline and the fibre/matrix interface respectively for each fibre. According to Figure 9, the principal stress in the 0˚ fibre is higher at the fibre mid-length and lower at fibre ends, and follows the characteristic shape as predicted by shear-lag theory [42]. This is further supported by the interfacial shear stress curve for the same fibre, which changes gradually from maximum negative shear at one end to maximum positive shear at the other

end. Similar curves are presented for the 45˚ fibre, but the stresses are lower due to the off-axis fibre orientation.

The *EMBEDDED ELEMENT technique does not discount the volume of the matrix where fibre elements are embedded, which artificially increases the effective fibre properties. Modified shear (G^*_F) and axial (E^*_F) moduli derived from Equation 4 are therefore used to compensate for this stiffening effect.

$G^*_F = G_F - G_M$, $\mathbf{E^*_F = E_F - E_M}$ **Equation 4**

where G_F and G_M are the original shear moduli of the fibre and matrix respectively, and E_F and E_M are the corresponding Young's moduli.

The seed size for the thickness of the matrix elements (z axis) was selected to be the same magnitude as the bundle thickness to ensure an appropriate host volume was captured for each embedded fibre element. The seed size for the fibre elements was approximately 12% of the measured dry bundle width. Identical values were chosen for the x-y plane of the matrix to maintain a 1:1 fibre to matrix ratio [25]. Following [8], a constant bundle Vf of 60% was used for the present work. A summary of the seed values used is outlined in Table 1.

Boundary conditions outlined in Table 4 have been applied to facilitate different loading conditions. Displacement controlled macroscopic loads are applied via the kinematically coupled reference node, ensuring the loaded surface follows the exact prescribed motion of the reference node (4% global strain for tensile and compressive load and 6% for shear load) -

a common approach amongst many authors [43-45]. Reference node reaction forces are evaluated at each time step by dividing the force over the loaded surface area to obtain the component stress. All rotational DOF (about the *X*, *Y* and *Z* axes) for the fibres are restricted [46], since only translational DOF of the embedded (fibre) element are constrained within the host (matrix) element (using *EMBEDDED ELEMENT). This prevents numerical singularities from occurring due to "ball-joint" effects.

3.2 Constituent material properties

Experimental data from [2] is used to provide input parameters for the FEA modelling in this paper. However, additional material properties are required due to the additional degrees of freedom used in this mixed-dimensional model, such as fibre bundle shear and transverse properties. Experimentally derived data for UD laminates has been collated from manufacturers' datasheets [47, 48] and experimental studies [2], as summarised in Table 3. These parameters are implemented using a user-defined material model (UMAT) in ABAQUS/Standard, based on a model previously developed by the authors in [2]. Failure criteria have also been incorporated into the UMAT to simulate progressive damage and enable ultimate strength predictions, using a continuum damage mechanics approach. If the stress state in the element exceeds the corresponding failure criterion then appropriate components within the stiffness matrix are degraded.

A simple Maximum Stress Criterion has been employed to identify fibre damage, where stress components S11 and S22 are considered independently. All direct and shear stiffness

components in the stiffness matrix are reduced to 1% of their original value if the failure criterion is violated. An interactive failure model (von Mises Stress Criterion) has been employed for the resin, which uses a single criterion to evaluate different modes of failure. This enables the introduction of non-linear, progressive damage into the matrix phase. There are three possible scenarios: undamaged, damaged (post elastic limit) and failed. The von Mises stress from each load increment is compared with the failure criterion to check for damage in tension, compression or shear. If no damage is present, the stiffness matrix is calculated using the initial elastic constants. However, if the elastic limit of the matrix is exceeded, the onset of damage occurs. Fracture or final failure is governed by a Maximum Strain Criterion. Final failure occurs if the maximum strain is exceeded and the stiffness matrix is reduced by the maximum degradation factor. For this case, the Young's modulus is degraded to 1% (d_E = 0.01) of the initial value and the shear modulus to 20% (d_G = 0.2) to account for frictional effects at the fracture interface [49]. If the onset of damage is detected, but final failure is not met, degradation factors are calculated to reduce the terms in the stiffness matrix. This case occurs when the yield strength (defined in this case as the onset of non-linearity on the stress/strain curve) has been exceeded, but the maximum ultimate strain criterion has not. The stiffness degradation (D) is governed by a damage parameter d, and a shape parameter n:

$$D = 1 - \frac{\left(\frac{\sigma_{Mises}}{\sigma_{matrix}} - 1\right)^n}{d} \qquad \textbf{Equation 5}$$

where σ_{Mises} denotes the von-Mises damage criterion and σ_{matrix} denotes the current von-Mises stress in the current time step. Previously performed regression analysis suggests that *d* is 10 and *n* is 1 for the current matrix system [2]. *D* is limited to a lower bound value of 1% for the direct stiffness components (d_E) and 20% for the shear components (d_G) to account for frictional effects at the fracture interface [49]:

$$d_E = \max(D, 0.01)$$
$$d_G = \max(D, 0.2)$$

Equation 6

The stiffness matrix at the relevant integration point is then recalculated for the isotropic matrix material as follows:

$$[C] = [S]^{-1} = \begin{bmatrix} \frac{1}{d_E E} & \frac{-\nu}{d_E E} & 0 \\ \frac{-\nu}{d_E E} & \frac{1}{d_E E} & 0 \\ 0 & 0 & \frac{1}{d_G G} \end{bmatrix}^{-1}$$

Equation 7

Further details of the UMAT and the stiffness degradation scheme can be found in [2].

4 Mechanical property determination

4.1 Damage initiation and progression

A von Mises stress contour plot is presented in Figure 10, for a 10% Vf RVE at a global applied tensile strain of 0.8%. As expected, bundles aligned parallel to the loading axis (*x* direction) exhibit the highest stress, since these fibres transfer a higher proportion of the tensile load. The tensile stress is lower at the bundle ends compared with the mid-length, which is consistent with shear lag theory [50] and the results presented in Figure 9.

Figure 11 presents damage parameter plots for an example tensile coupon of 12K, 36mm long bundles at 10% Vf. The RVE dimensions were 38x38x3mm, which was subjected to a tensile load in the x-direction. Each damage mode is recorded using a separate state variable (STATEV) in ABAQUS/Standard, enabling the mode of failure to be investigated in more detail. Figure 11a shows the entire damage plot (0.8% applied strain) prior to final failure. It indicates that large areas of matrix elements have become damaged (green regions) prior to final coupon failure, which corresponds with audible cracking witnessed during experimental testing. Failure is therefore progressive and is dominated by transverse bundle failure (see Figure 11b), as previously reported in [51]. Additional bundles fail in shear as the applied strain develops, as shown in Figure 11c. Transverse bundle failure is a common failure mode for DFCs under tensile loading due to the significantly weaker transverse properties (70MPa) compared with the longitudinal properties (2893MPa – see Table 3), causing filaments to separate along the

longitudinal bundle axis. This is an important failure mode captured by the current model, which is overlooked when representing the bundles as 1D beam elements [7, 22-26].

Tensile stress/strain curves from the FEA simulations are compared against experimental data[2] in Figure 12 for two fibre volume fractions. The curves closely match in terms of initial stiffness, onset of non-linearity, ultimate strength and ultimate strain. Simulated strain to failure values are within 15% of the experimental samples at volume fractions of 30% (~13%) and 50% (~15%). This is considered to be a good level of agreement, considering the same level of experimental error is reported for DFC materials in [52, 53]. These results demonstrate the importance of characterising the non-linearity of the matrix material and support the damage evolution described above.

Compressive and shear stress/strain curves from the FEA simulations are compared against experimental data [54] in Figure 13. There is good agreement between the simulations and experimental results in terms of the elastic stiffnesses. There is approximately a 2.5% error between the experimental data and the simulation data for the compressive stiffness and 7% for the shear stiffness. For the ultimate compressive strength, the predicted values are within 20% of the experimental results, where the largest contributing factor is the lack of fibre buckling in the proposed implicit FE model, which is a common failure mode observed in the experimental specimens. For the ultimate shear strength, the error between the numerical and experimental values increases to ~40%, which is due to the simplified interfacial region, assuming perfect bonding with the embedded element approach.

4.2 Comparison with 2D approach

FEA tensile moduli and strengths predicted using the current 3D model are directly compared in this section against experimental data [2] and the 2D model presented in [25]. Five repeat simulations have been performed for each scenario and the results are presented in Figure 14. RVEs featuring 36mm long, 12K fibres were generated for a range of volume fractions. All three data sets in Figure 14 confirm that there is a linear relationship between the volume fraction and the tensile modulus. It should also be noted that although tensile moduli are presented for volume fractions of up to 60% in Figure 14, the practical upper limit for random DFC is 50%-55% [2]. Higher volume fractions result in poor fibre impregnation, hence large reduction in material properties, which is indicated by the experimental data point at 57% Vf in Figure 14. According to Figure 14, tensile modulus predictions using the 2D and 3D models yield similar results, with less than 5% error for all volume fractions considered. Both models show good agreement with the experimental data at volume fractions between 40%-45% (within 5% for the 3D shell model and within 3% for the 2D beam model), but errors increase for both models (up to 30%) for volume fractions greater than 50%. A possible cause for this increase in error is the oversight of tow fragmentation in the current model, which has been reported to increase the tensile modulus by up to 13% compared to unfilamentised bundled materials [55], as it improves the homogeneity.

UTS predictions are compared and benchmarked against experimental data in Figure 15. The UTS also follows a strong linear relationship with the volume fraction for all three curves. UTS

values predicted by the 2D model are closer to the experimental data at a volume fraction of 35%, but the 3D model provides closer agreement at higher volume fractions (up to 4.2% for the 3D model and up to 18% for the 2D model over 40% Vf). At lower volume fractions (<30%), UTS values predicted by the 2D model are generally lower than those predicted by the 3D model, possibly because of the poor representation of the fibre areal coverage resulting from using 1D beams to represent the ribbon-like fibre bundles. At higher volume fractions (>30%), 2D models tend to over-predict the UTS because some of the important failure mechanisms such as transverse bundle failure and in-plane bundle shear cannot be captured using these models. Additionally, the 3D model takes into account the effect of out-of-plane fibre curvature, which significantly affects the load carrying capability of the fibres. This becomes more significant as the fibre volume fraction increases and the fibres bend/distort to pack into the available cavity volume.

It should be noted that in Figure 14 and Figure 15, the main sources of variability for the experimental data can be attributed to variations in fibre architecture (local volume fraction and fibre orientation), variations in constituent material properties and defects from manufacturing (such as voids and dry-spots). Whereas, the numerical predictions currently only account for variations in the fibre architecture, and the pre-processor always ensures the target volume fraction is reached. Therefore, error bars for the predicted tensile modulus and UTS are generally smaller than for the experimental results.

4.3 Effects of RVE thickness

A range of RVEs of varying thickness (1.5mm, 3mm, 4.5mm and 6mm) have been generated in order to demonstrate the thickness size effect present in DFCs. All fibre architectures consisted of 12K, 36mm long fibres. According to Figure 16, the tensile modulus follows a bi-linear relationship with increasing RVE thickness. A critical thickness occurs at 3mm for the geometry investigated, after which the modulus reaches a maximum. This bi-linear relationship was also observed in [14], for DFC samples consisting of a different fibre architecture (6K, 57.5mm long bundles at 30% Vf).

The predicted UTS for the 12K, 36mm DFC architecture appears to increase linearly from 1.5mm to 6mm, while the experimental UTS shows a bi-linear relationship. Comparisons between the curves suggest that the UTS is more sensitive to size effects (increasing coupon thickness) than the tensile modulus. Whilst the tensile modulus is a volume averaged material property, the UTS is more susceptible to defects and irregularities in the heterogeneous fibre architecture. As the RVE thickness decreases, it becomes increasingly difficult to achieve homogeneous fibre coverage and local areal mass variations become more significant.

5 Conclusions

A numerical model has been developed to characterise a number of meso-scale, discontinuous fibre architectures. Three numerical algorithms were integrated to produce a network of non-contacting fibres. Fibre kinematics, such as fibre bending and twist during compaction were

simulated to produce realistic levels of fibre tortuosity observed in moulded samples. The model has been demonstrated to produce RVEs with higher fibre volume fractions (~50%) compared with conventional hard-core models presented in the literature.

A custom Delaunay meshing algorithm has been adopted to mesh the RVE fibre architecture for FEA. The model has been adopted in this paper to predict the tensile, compressive and in-plane shear properties of DFCs, using a UMAT subroutine to simulate progressive damage of the constituent materials. For tensile samples, in-plane bundle shear and transverse tensile bundle failure were the critical failure modes, which were in agreement with experimental observations. Tensile modulus predictions were in close agreement with experimental data (less than 5% error) at volume fractions between 40%-45%, but the error increased to ~30% at volume fractions approaching 55%. Ultimate tensile strength predictions were within ~4.2% of the experimental data at volume fractions between 40%-55%. Whilst the error in the tensile modulus prediction increases marginally (from 3% to 5%) using the 3D model over the existing 2D beam model, the error in the UTS predictions is significantly reduced (from 18% to 4.2%). This highlights the importance of capturing the dominant failure mechanisms and the influence of out-of-plane fibres using the 3D model. Larger errors were reported for the ultimate compressive strength (20%) and shear strength (40%) predictions, as some of the dominant failure modes were overlooked by the current continuum damage model.

6 Acknowledgements

This work formed part of the Towards Affordable, Closed-Loop Recyclable Future Low Carbon Vehicle Structures (TARF-LCV) project, funded by the UK Engineering and Physical Sciences Research Council, EPSRC (reference EP/I038616/1). The authors would also like to thank Bentley Motors Limited for their continued financial and technical support.

7 References

1. Feraboli, P., T. Cleveland, P. Stickler, and J. Halpin, *Stochastic laminate analogy for simulating the variability in modulus of discontinuous composite materials.* Composites Part A: Applied Science and Manufacturing, 2010. **41**(4): p. 557-570.
2. Luchoo, R., L.T. Harper, M.D. Bond, N.A. Warrior, and A. Dodworth, *Net-shape spray deposition for compression moulding of discontinuous fibre composites for high performance applications* Plastics, Rubber and Composites: Macromolecular Engineering, 2009. **39**(3-5): p. 216-231.
3. Aubry, J., *HexMC — bridging the gap between prepreg and SMC.* Reinforced Plastics, 2001. **45**(6): p. 38-40.
4. Blumentrit, B.F., B.T. Vu, and S.L. Cooper, *The mechanical properties of oriented discontinuous fiber-reinforced thermoplastics. 1. Unidirectional fiber orientation.* Polymer Engineering and Science, 1974. **14**: p. 633-640.
5. Feraboli, P., E. Peitso, F. Deleo, T. Cleveland, and P.B. Stickler, *Characterization of Prepreg-Based Discontinuous Carbon Fiber/Epoxy Systems.* Composite Materials Technology, 2008: p. 289-299.
6. Maalej, M., *Tensile properties of short fiber composites with fiber strength distribution.* Journal of Materials Science, 2001. **36**: p. 2203-2212.
7. Harper, L.T., C. Qian, T.A. Turner, S. Li, and N.A. Warrior, *Representative volume elements for discontinuous carbon fibre composites – Part 2: Determining the critical size.* Composites Science and Technology, 2012. **72**(2): p. 204-210.
8. Harper, L.T., T.A. Turner, N.A. Warrior, and C.D. Rudd, *Characterisation of random carbon fibre composites from a directed fibre preforming process: Effect of fibre length.* Composites Part A: Applied Science and Manufacturing, 2006. **37**(11): p. 1863-1878.
9. Wisnom, M.R., *Size effects in the testing of fibre-composite materials.* Composites Science and Technology, 1999. **59**: p. 1937-1957.

10. Sutherland, L.S., R.A. Shenoi, and S.M. Lewis, *Size and scale effects in composites: I. Literature review.* Composites Science and Technology, 1999. **59**(2): p. 209-220.
11. Gitman, I.M., H. Askes, and L.J. Sluys, *Representative volume: Existence and size determination.* Engineering Fracture Mechanics, 2007. **74**: p. 2518-2534.
12. Kanit, T., S. Forest, I. Galliet, V. Mounoury, and D. Jeulin, *Determination of the size of the representative volume element for random composites: statistical and numerical approach.* International Journal of Solids and Structures, 2003. **40**: p. 3647-3679.
13. Tuttle, M., T. Shifman, and B. Boursier, *Simplifying certification of discontinuous composite material forms for primary aircraft structures.*, in *SAMPE Conference* 2010: Seattle.
14. Qian, C.C., L.T. Harper, T.A. Turner, and N.A. Warrior, *Structural optimisation of random discontinuous fibre composites: Part 1 – Methodology.* Composites Part A: Applied Science and Manufacturing, 2015. **68**: p. 406-416.
15. Baker, A., S. Dutton, and K. Donald, *Composite Materials for Aircraft Structures (2nd Edition)*. 2004: American Institute of Aeronautics and Astronautics.
16. Pan, Y., *Stiffness and progressive damage analysis on random chopped fiber composite using FEM*. 2010, The State University of New Jersey: New Brunswick.
17. Kari, S., *Micromechanical Modelling and Numerical Homogenization of Fibre and Particle Reinforced Composites*, in *Institute of Mechanics Department*. 2005, Otto-von-Guericke University Magdeburg: Magdeburg.
18. Faessel, M., C. Delisee, F. Bos, and P. Castera, *3D Modelling of random cellulosic fibrous networks based on X-ray tomography and image analysis.* Composites Science and Technology, 2005. **65**: p. 1931-1940.
19. Hill, R., *Elastic properties of reinforced solids: some theoretical principles.* Journal of the Mechanics and Physics of Solids, 1963. **11**: p. 357.
20. Altendorf, H., *3D Morphological Analysis and Modeling of Random Fiber Networks*, in *École doctorale nO432: Sciences des Métiers de l'Ingénieur*. 2011, l'École Nationale Supérieure des Mines de Paris: Paris.
21. Williams, S.R. and A.P. Philipse, *Random packings of spheres and spherocylinders simulated by mechanical contraction.* Physical Review E, 2003. **67**(5): p. 051301.
22. Elahi, M. and Y.J. Weitsman, *On the mechanical response of chopped glass/urethane resin composite: Data and model*. 1999, Oak Ridge National Laboratory. p. 61.
23. Eason, T. and O. Ochoa, *Modeling residual stresses and damage initiation in discontinuous random fiber SRIM composites.* Computer Aided Design in Composite Material Technology, 1996. **5**: p. 123-132.
24. Eason, T. and O. Ochoa, *Material behaviour of Structural Reaction Injection Molded composites under thermomechanical loading.* Journal of Composite Materials, 2000. **34**(5): p. 411-432.
25. Harper, L.T., C. Qian, T.A. Turner, S. Li, and N.A. Warrior, *Representative volume elements for discontinuous carbon fibre composites – Part 1: Boundary conditions.* Composites Science and Technology, 2012. **72**(2): p. 225-234.

26. Wu, X.-F. and Y.A. Dzenis, *Elasticity of planar fiber networks.* Journal of Applied Physics, 2005. **98**.
27. Dirrenberger, J., S. Forest, and D. Jeulin, *Towards gigantic RVE sizes for 3D stochastic fibrous networks.* International Journal of Solids and Structures, 2014. **51**(2): p. 359-376.
28. Pan, Y., L. Iorga, and A.A. Pelegri, *Analysis of 3D random chopped fiber reinforced composites using FEM and random sequential adsorption.* Computational Materials Science, 2008. **43**(3): p. 450-461.
29. Pan, Y., L. Iorga, and A.A. Pelegri, *Numerical generation of a random chopped fiber composite RVE and its elastic properties.* Composites Science and Technology, 2008. **68**(13): p. 2792-2798.
30. Velmurugan, R., G. Srinivasulu, and S. Jayasankar, *Influence of fiber waviness on the effective properties of discontinuous fiber reinforced composites.* Computational Materials Science, 2014. **91**(0): p. 339-349.
31. Luchoo, R., L.T. Harper, N.A. Warrior, and A. Dodworth, *Three-dimensional numerical modelling of discontinuous fibre composite architectures.* Plastics, Rubber and Composites, 2011. **40**(6/7): p. 356-362.
32. Cuilliere, J.C., S. Bournival, and V. Francois, *A mesh-geometry-based solution to mixed-dimensional coupling.* Computer-Aided Design, 2010. **42**: p. 509-522.
33. Liang, Y.-D. and B.A. Barsky, *A New Concept and Method for Line Clipping.* ACM Trans. Graph., 1984. **3**(1): p. 1-22.
34. Liang, Y.-D., B.A. Barsky, and M. Slater, *Some Improvements to a Parametric Line Clipping Algorithm*. 1992, EECS Department, University of California, Berkeley.
35. EVANS, K.E. and M.D. FERRAR, *The packing of thick fibres.* Journal of Physics D: Applied Physics, 1989. **22**: p. 354-360.
36. Sherburn, M., *Geometric and Mechanical Modelling of Textiles*, in *The School of Mechanical, Materials and Manufacturing Engineering*. 2007, The University of Nottingham: Nottingham.
37. Birbil, S.I. and S.C. Fang, *An Electromagnetism-like Mechanism for Global Optimization.* Journal of Global Optimization, 2003. **25**: p. 263-282.
38. Harper, L.T., T.A. Turner, N.A. Warrior, J.S. Dahl, and C.D. Rudd, *Characterisation of random carbon fibre composites from a directed fibre preforming process: Analysis of microstructural parameters.* Composites Part A: Applied Science and Manufacturing, 2006. **37**(11): p. 2136-2147.
39. Catmull, E. and R. Rom, *A Class of Local Interpolating Splines*, in *Computer Aided Geomtric Design*. 1974, Academic Press, Inc.: Salt Lake City.
40. Luchoo, R., L.T. Harper, M.D. Bond, N.A. Warrior, and A. Dodworth, *Net shape spray deposition for compression moulding of discontinuous fibre composites for high performance applications* Plastics, Rubber and Composites, 2010. **39**: p. 216-231.
41. Hine, P.J., H.R. Lusti, and A.A. Gusev, *Numerical simulation of the effects of volume fraction, aspect ratio and fibre length distribution on the elastic and thermoelastic*

properties of short fibre composites. Composites Science and Technology, 2002. **62**: p. 1445-1453.
42. COX, H.L., *The elasticity and strength of paper and other fibrous materials.* British Journal of Applied Physics, 1952. **3**: p. 72-79.
43. HBAIEB, K., Q.X. WANG, Y.H.J. CHIA, and B. COTTERELL, *Modelling Siffness of Polymer/Clay Nanocomposites.* Polymer 2007. **48**: p. 901-909.
44. DUSCHLBAUER, D., H.J. BÖHM, and H.E. PETTERMANN, *Computational Simulation of Composites Reinforced by Planar Random Fibers: Homogenization and Localization by Unit Cell and Mean Field Approaches.* Journal of Composite Materials, 2006. **40**.
45. POTLURI, P. and T.V. SAGAR, *Compaction modelling of textile preforms for composite structures.* Composite Structures, 2008. **86**(177-185): p. 177.
46. *Abaqus 6.8-3 Documentation - Abaqus Analysis User's Manual*. 2008, Dessault Systéms.
47. SODEN, P.D., M.J. HINTON, and A.S. KADDOUR, *Lamina properties, lay-up configurations and loading conditions for a range of fibre-reinforced composite laminates.* Composites Science and Technology, 1998. **58**: p. 1011-1022.
48. TORAYCA. *T700S DATA SHEET*. [Material Technical Data sheet] 18/04/2013; Available from: http://www.toraycfa.com/pdfs/T700SDataSheet.pdf
49. Blacketter, D.M., D.E. Walrath, and A.C. Hansen, *Modelling damage in a plain weave fabric-reinforced composite material.* Journal of Composites Technology and Research, 1993. **15**(2): p. 136-142.
50. Kelly, A. and W.R. Tyson, *Tensile properties of fibre-reinforced metals: Copper/Tungsten and Copper/Molybdenum.* Journal of the Mechanics and Physics of Solids, 1965. **13**: p. 329-350.
51. Feraboli, P., E. Peitso, F. Deleo, T. Cleveland, and P.B. Stickler, *Characterization of Prepreg-Based Discontinuous Carbon Fiber/Epoxy Systems.* Journal of Reinforced Plastics and Composites, 2009. **28**.
52. Harper, L.T., T.A. Turner, J.R.B. Martin, and N.A. Warrior, *Fiber Alignment in Directed Carbon Fiber Preforms - Mechanical Property Prediction.* Journal of Composite Materials, 2010. **44**(8): p. 931-951.
53. Qian, C., L.T. Harper, T.A. Turner, and N.A. Warrior, *Notched behaviour of discontinuous carbon fibre composites: Comparison with quasi-isotropic non-crimp fabric.* Composites Part A: Applied Science and Manufacturing, 2011. **42**(3): p. 293-302.
54. HARPER, L.T., *Discontinuous carbon fibre composites for automotive applications*, in *PhD Thesis*. 2006, The University of Nottingham: Nottingham.
55. HARPER, L.T., T.A. TURNER, N.A. WARRIOR, and C.D. RUDD, *Characterisation of random carbon fibre composites from a directed fibre preforming process: The effect of tow filamentisation.* Composites: Part A: Applied Science and Manufacturing, 2007. **38**(3): p. 755-770.
56. TORAYCA, *T700S DATA SHEET*. TORAY CARBON FIBERS AMERICA, INC.
57. HEXCEL, *HexTow AS4 Carbon Fibre - Product Data*. 2010, Hexcel Corporation.

58. BOND, M.D., *Multi-Scale Modelling of Discontinuous Carbon Fibre Reinforced Composites*, in *Mechanics, Materials and Structures*. 2012, The University of Nottingham: Nottingham.

8 Tables

Table 1: Fibre and resin element seed values used for a range of bundle sizes. Bundle widths were measured from dry bundles, rather than from moulded plaques.

Fibre Bundle Size	Measured dry bundle width (mm)	Assumed bundle Vf	Impregnated bundle thickness (mm)	Fibre seed (mm)	Resin seed x-direction (mm)	Resin seed y-direction (mm)	Resin seed z-direction (mm)
3K	1.71	60%	0.11	0.205	0.205	0.205	0.11
6K	3.26	60%	0.12	0.391	0.391	0.391	0.12
12K	5.25	60%	0.15	0.63	0.63	0.63	0.15
24K	6.1	60%	0.25	0.732	0.732	0.732	0.25

Table 2: Summary of the spring constants used for RVE generation.

Node Charge $k_{REPULSION}$ (N.mm^2)	Parent axial $K_{PARENT-AX}$ (N/mm)	Parent rotational $K_{PARENT-RT}$ (N.rad)	Sister axial $k_{SISTER-AX}$ (N/mm)	Sister rotational $k_{SISTER-RT}$ (N.rad)
12	1050	27000	1600	27000

Table 3: Carbon fibre bundle properties. Figures in brackets represent modified properties used for all FEA simulations (to account for volume added effects using embedded element approach).

E^T_1 (GPa)	E^T_2 (GPa)	E^C_1 (GPa)	E^C_2 (GPa)	G_{12} (GPa)	σ^T_1 (MPa)	σ^T_2 (MPa)	σ^C_1 (MPa)	σ^C_2 (MPa)	σ^S_{12} (MPa)	υ_{12}	υ_{23}
125*	11**	128***	11^	6.6**	2839.03	70*	1570*	200**	98*	0.28**	0.4**
(121.65)	(7.65)	(120.47⊥)	(3.47⊥)	(5.39)							

*T700 – Manufacturer's data sheet [56], ** AS4 – Experimentally derived in [47], ***AS4 – Manufacturer's data sheet [57],

^Transverse compressive modulus was assumed to be identical to transverse Young's modulus since no data was available,

⊥Modified compressive moduli were calculated using experimentally derived compressive resin properties [58]

Table 4: Summary of boundary conditions employed for FEA simulations (For notation see Figure 8)

	Node/Surface/Element	Boundary Conditions
TENSION/COMPRESSION	Node A	Encastre
	Node D	$u_z = 0$
	Surface ABCD	$u_x = 0$
	Surface EFGH	u_x = Reference node
	Fibre elements (1D beams)	$\omega_x = \omega_y = \omega_z = 0$
	Reference Node	u_x = +/-0.04* l_{RVE} where l_{RVE} = absolute distance between nodes A-E
SHEAR	Node A	Encastre
	Node D	$u_z = 0$
	Surface ABEF	$u_x = 0$
	Surface CDGH	$u_x = 0$
	Surface ABCD	$u_x = 0$, $u_y = 0$
	Surface EFGH	$u_x = 0$, u_y = Reference node
	Reference Node	u_y = 0.06* l_{RVE} where l_{RVE} = absolute distance between nodes A-E

9 Figures

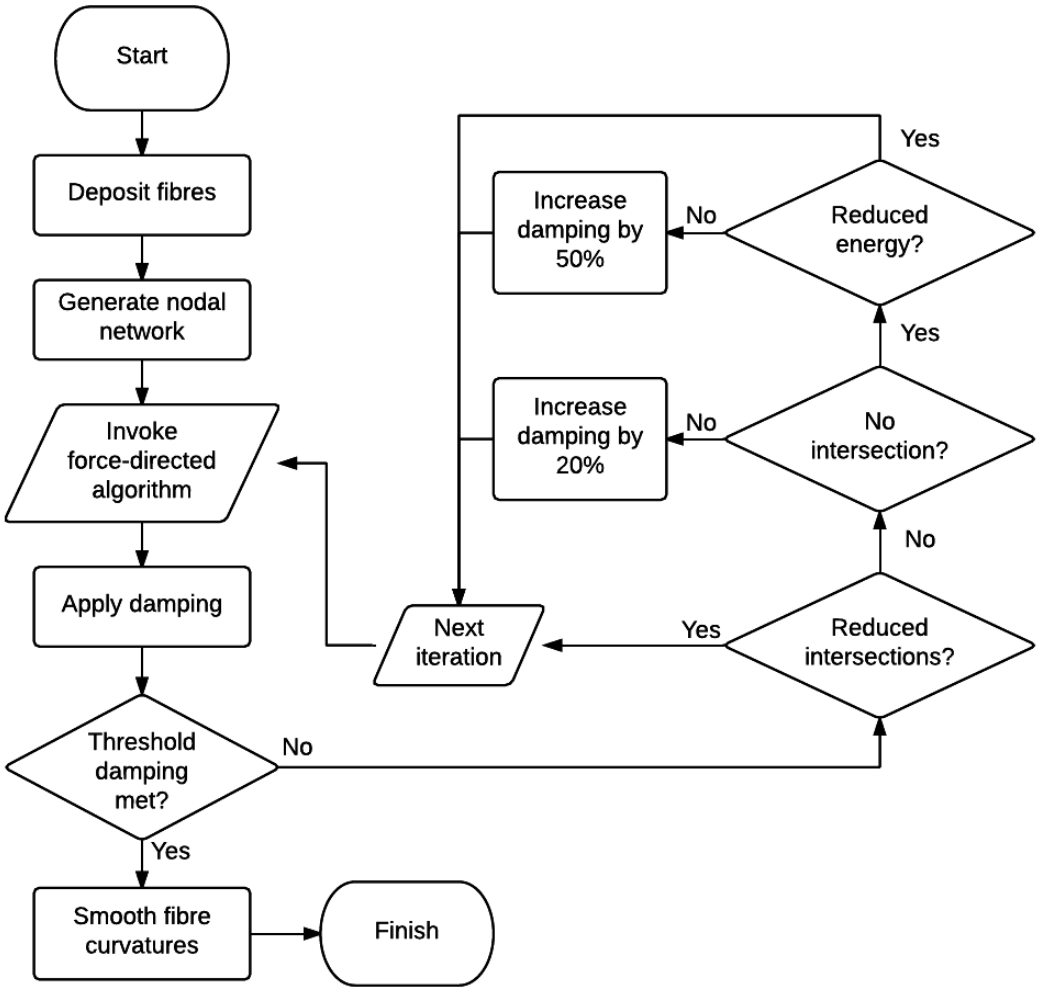

Figure 1: Process flowchart of the RVE generation program

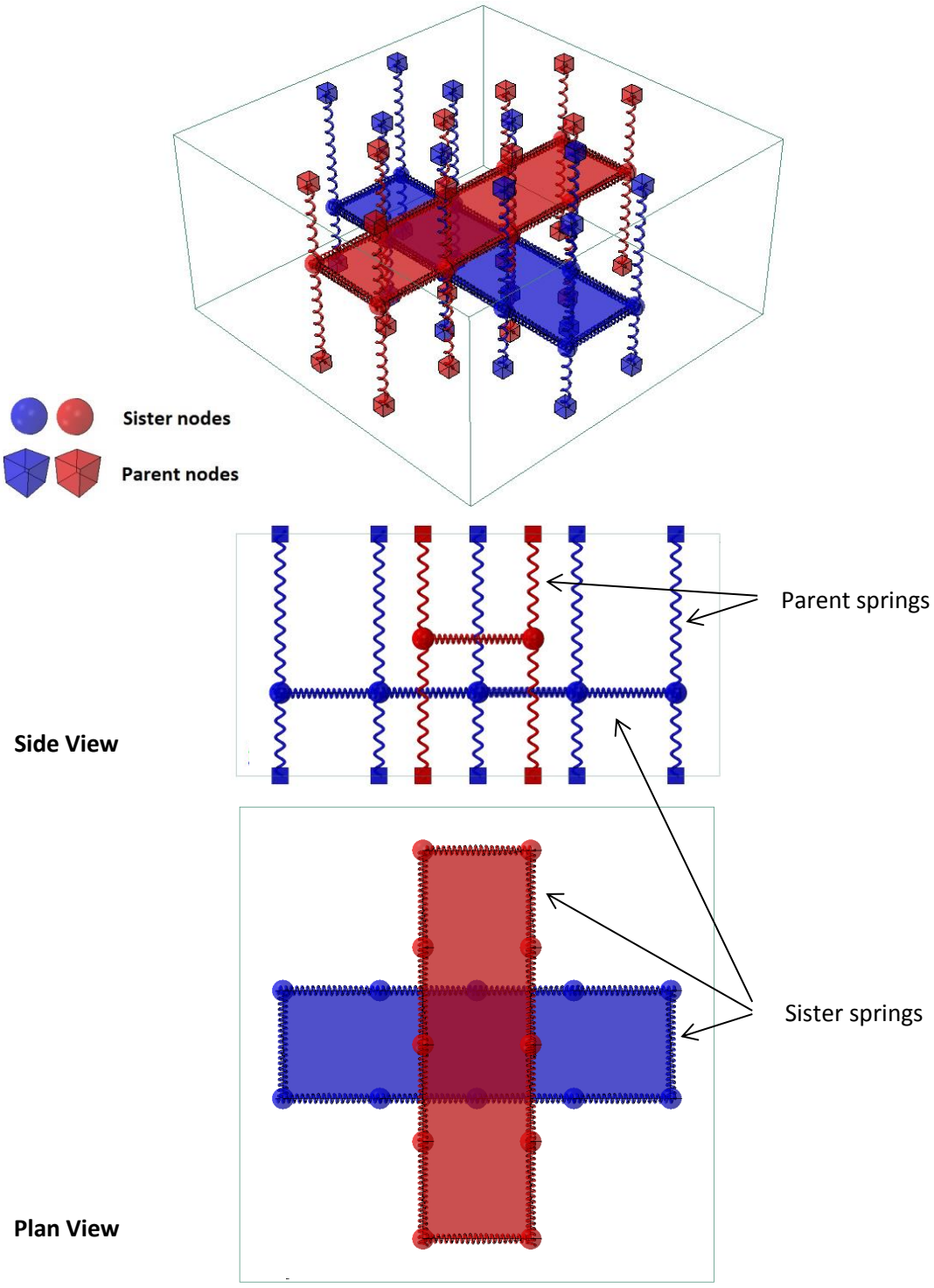

Figure 2: Initial nodal network for two non-intersecting fibre bundles

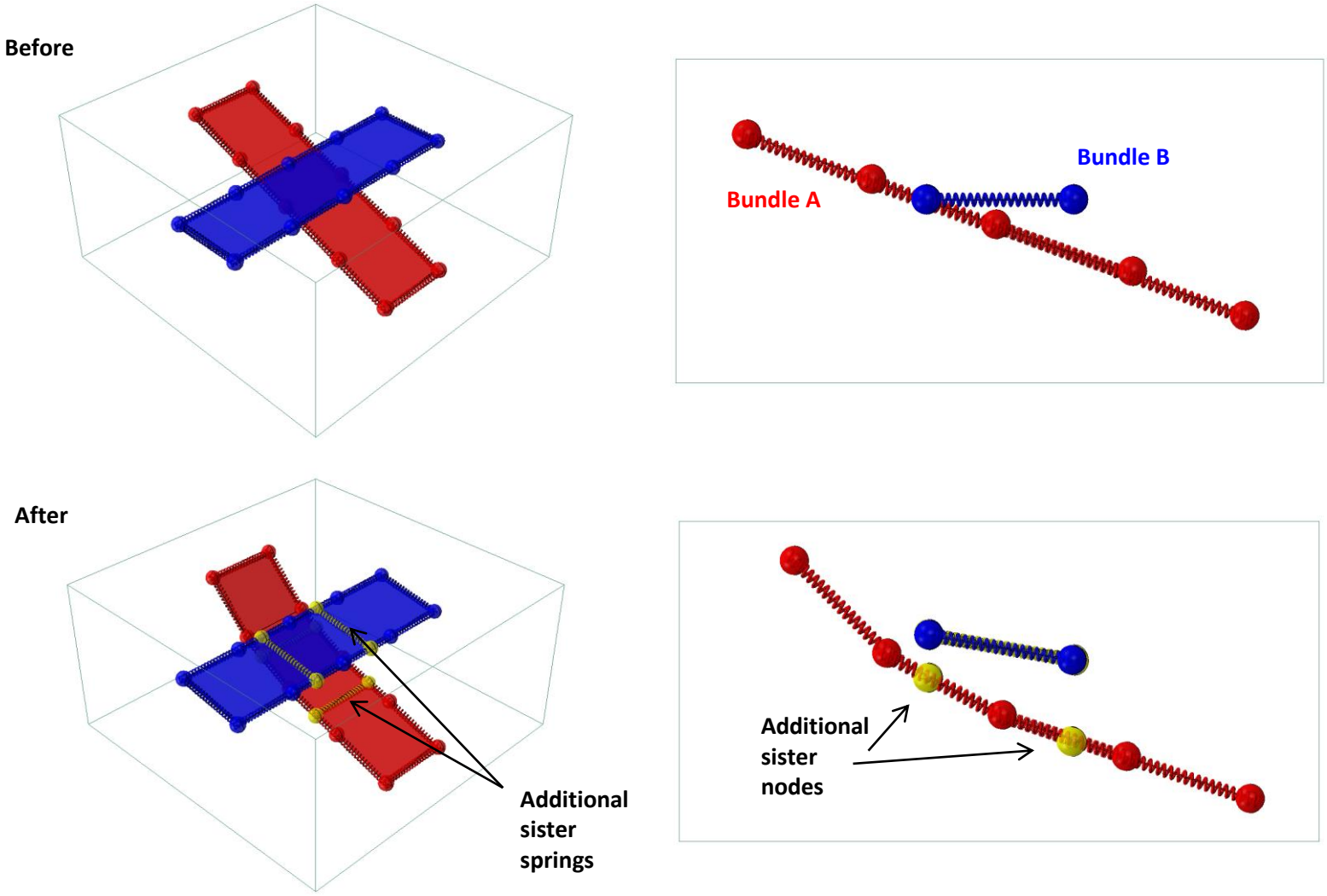

Figure 3: Schematic of edge-edge intersection, before and after intersection-elevation algorithm is applied (parent nodes and springs removed for clarity)

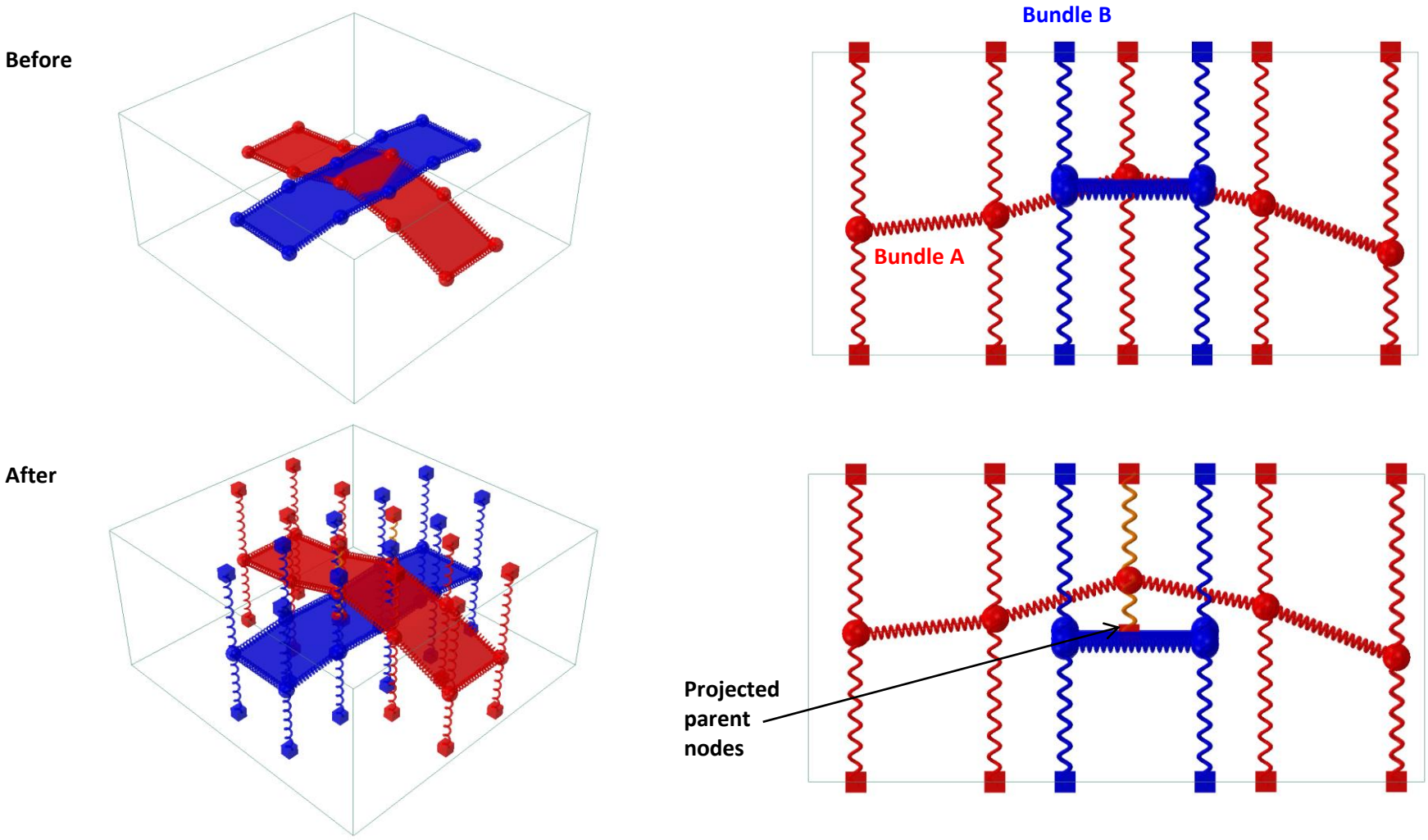

Figure 4: Schematic of edge-surface intersection before and after intersection-elevation algorithm is applied (parent nodes and springs removed in top right image for clarity)

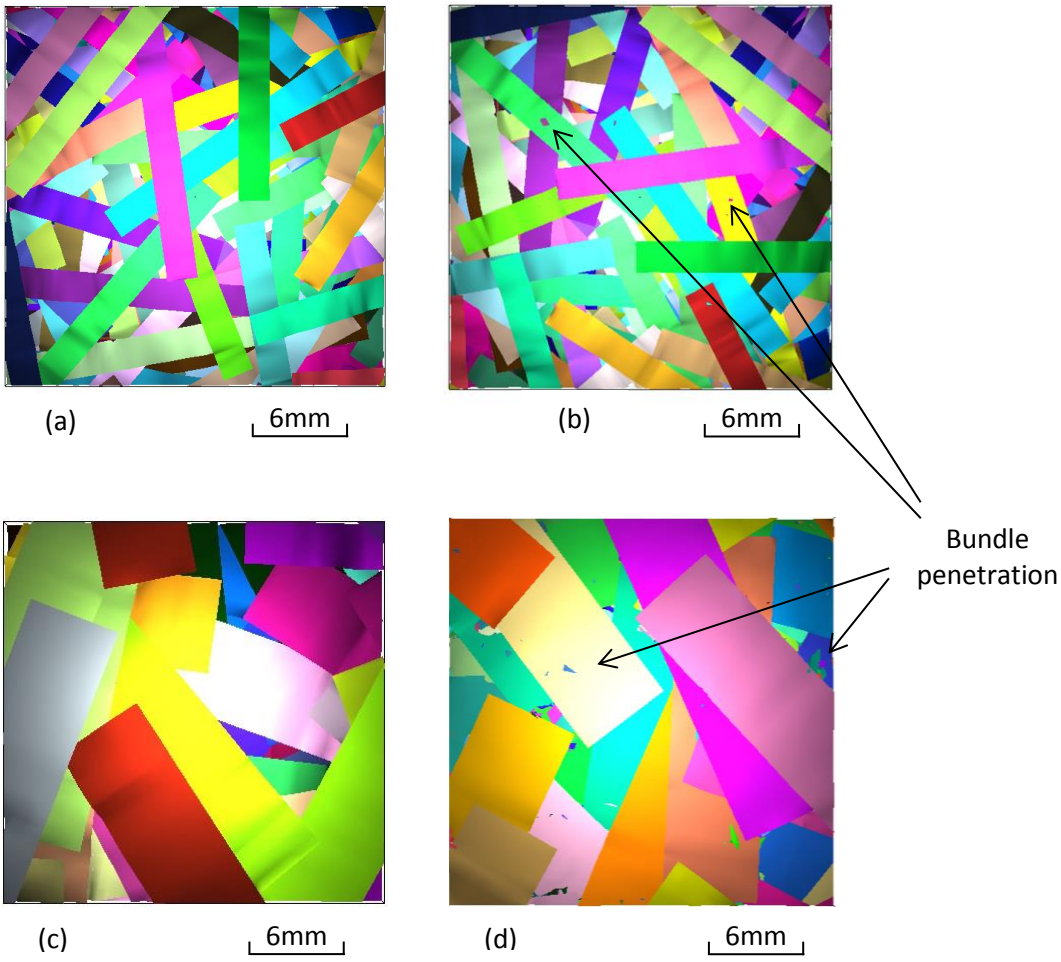

Figure 5: Example RVE architectures generated from the numerical model using the optimised parameters from Table 2. A nominal fibre length of 30mm is used with bundles sizes (a) 6k 30%Vf, (b) 6k 60%Vf, (c) 24k 30%Vf, (d) 24k 60%Vf.

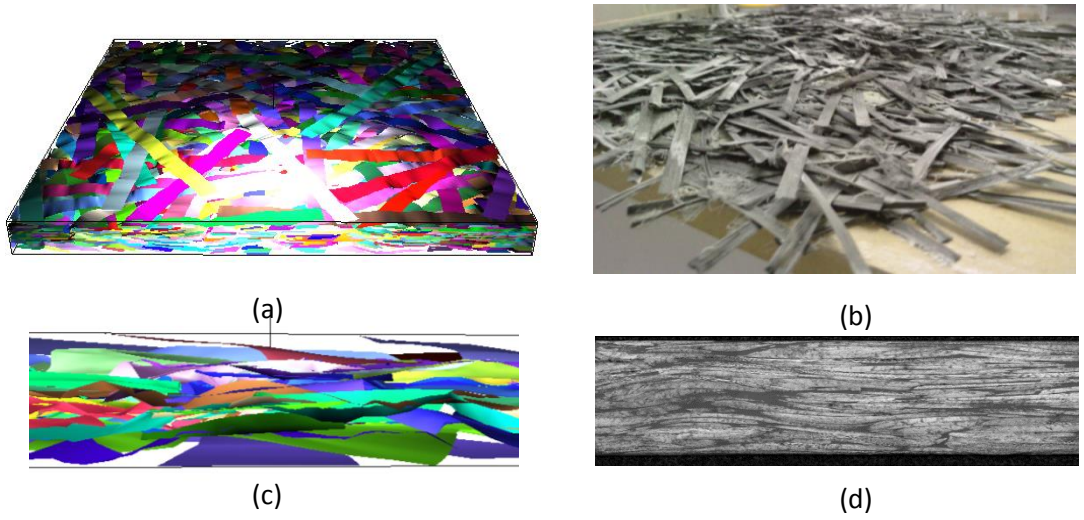

Figure 6: Comparisons of DFP fibre architectures consisting of 6k, 36mm fibre bundles. (a) DPF fibre architecture generated using the current model. (b) DFP preform produced using automated fibre deposition process. (c) Close up view from the side of (a). (d) Micrograph of a specimen taken from (b) after moulding.

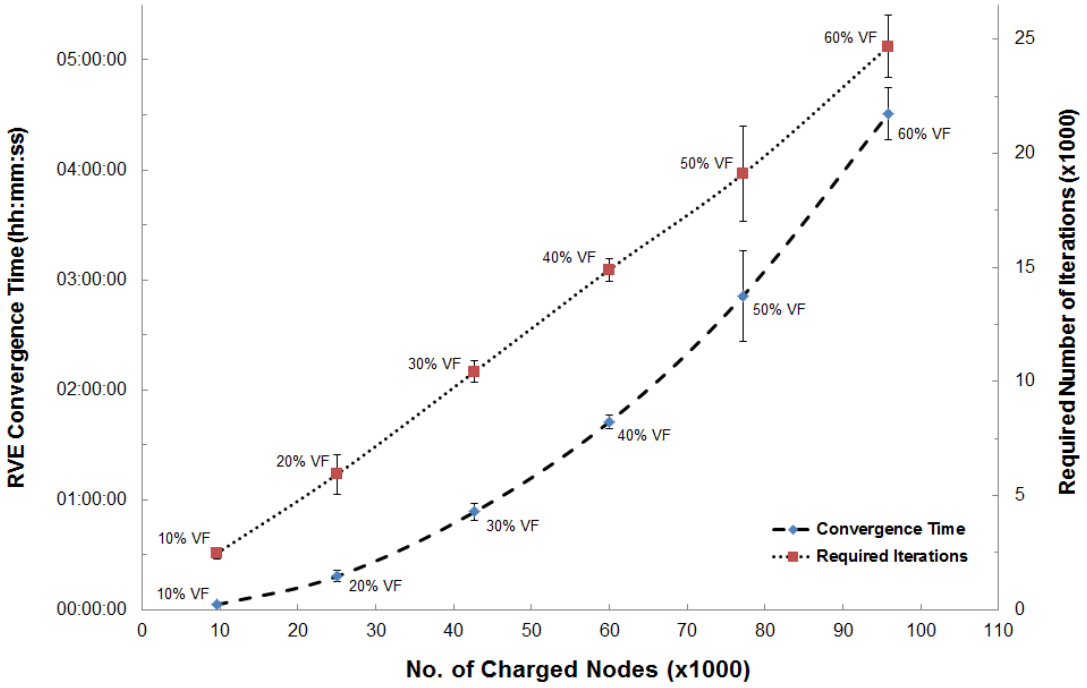

Figure 7: Effect of volume fraction on convergence time and number of iterations. All data are obtained using a 38x38x3mm cell consisting of 36mm, 12K fibres.

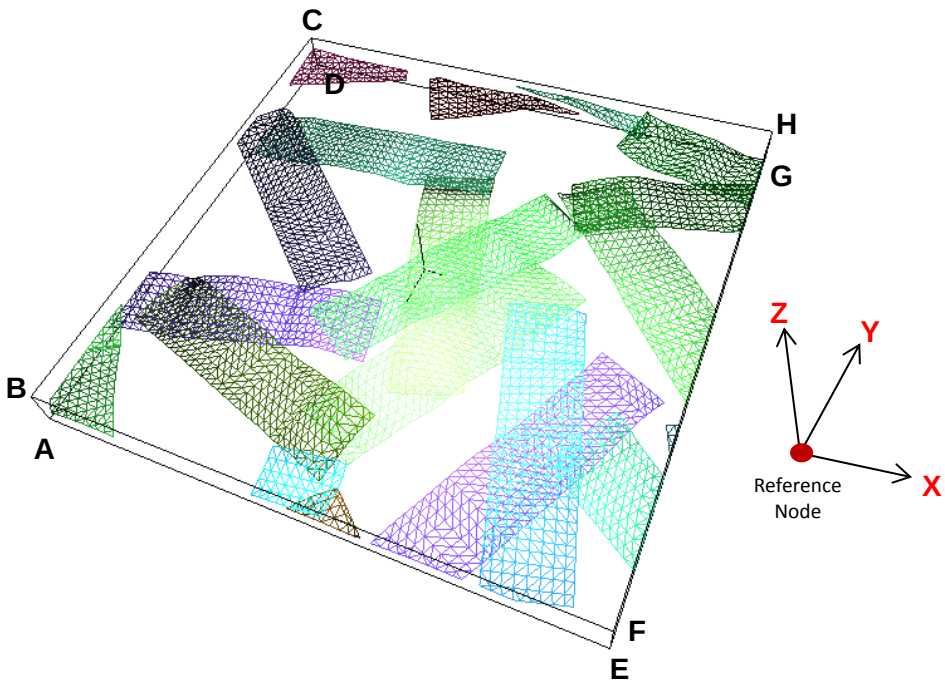

Figure 8: Example meshed fibre architecture (40x40x3mm RVE with 30mm 12K fibres). A dilute fibre volume fraction (<5%) has been selected for illustration purposes.

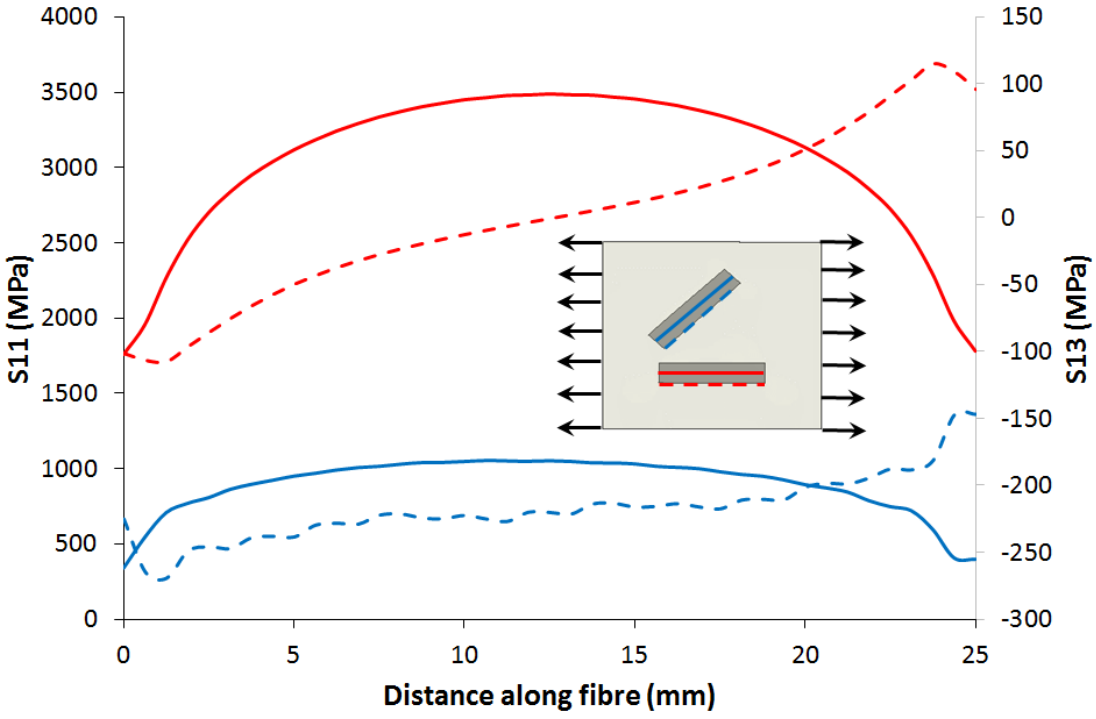

Figure 9: Principal stress (S11) distribution and interfacial shear stress (S12) distribution along the length of two fibres at 0˚ and 45˚ to the loading direction. Solid lines represent S11 taken from the fibre centrelines and dashed lines represent S12 taken from fibre edges.

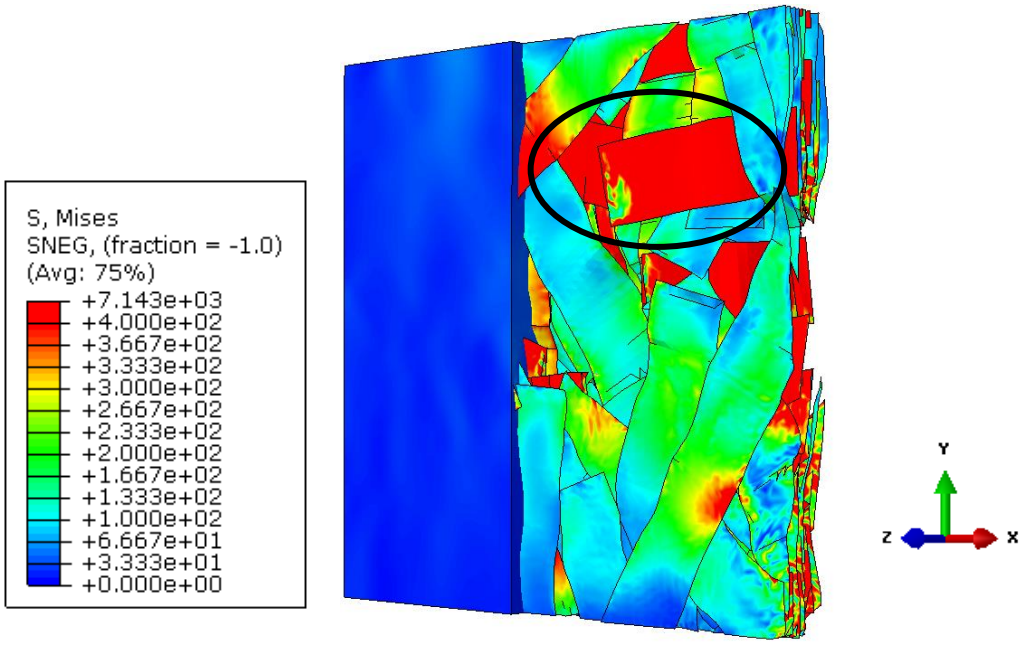

Figure 10: von Mises plot for a 10% Vf, 38x38x3mm RVE at a global applied tensile strain of 0.8% in the x-direction (prior to coupon failure). Plot scaled between 0-400MPa to highlight stress in fibre. Section of resin removed to display internal fibres. Black circle highlights highly stressed fibre along loading direction.

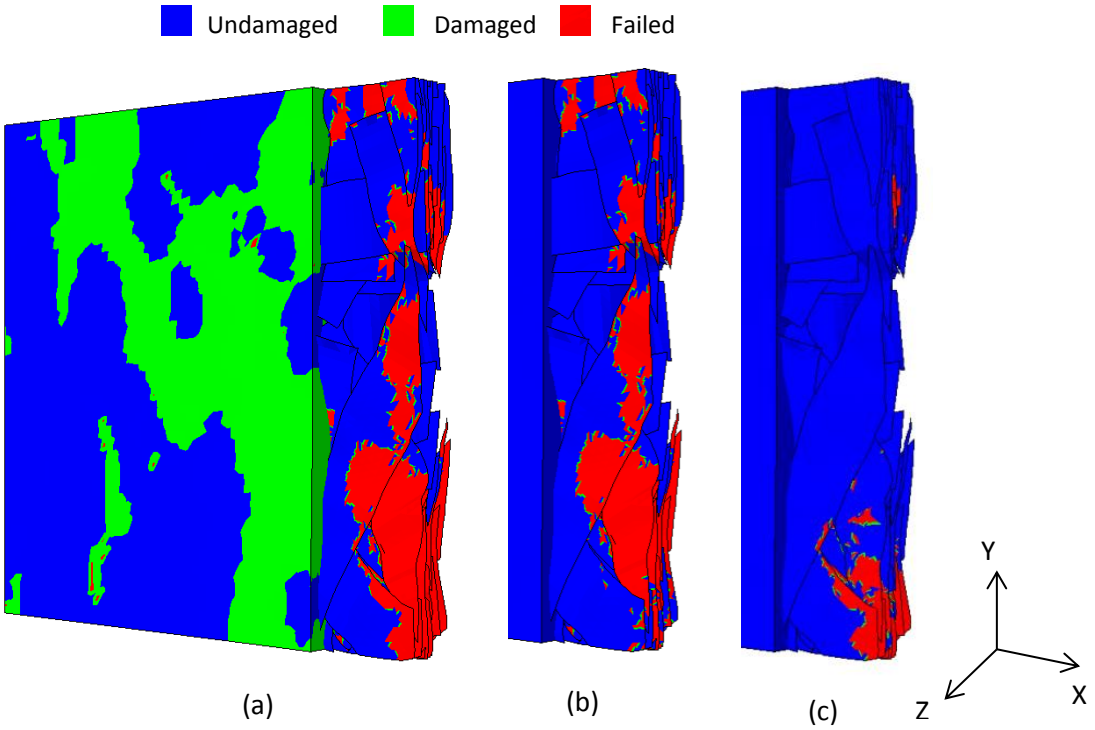

Figure 11: Damage parameter plot for a 10% Vf, 38x38x3mm RVE at a global applied strain of 0.8% (prior to coupon failure). Damage plots illustrate (a) all damage modes; (b) transverse bundle failure only and (c) in-plane bundle shear only. (Section of resin removed to display internal fibres).

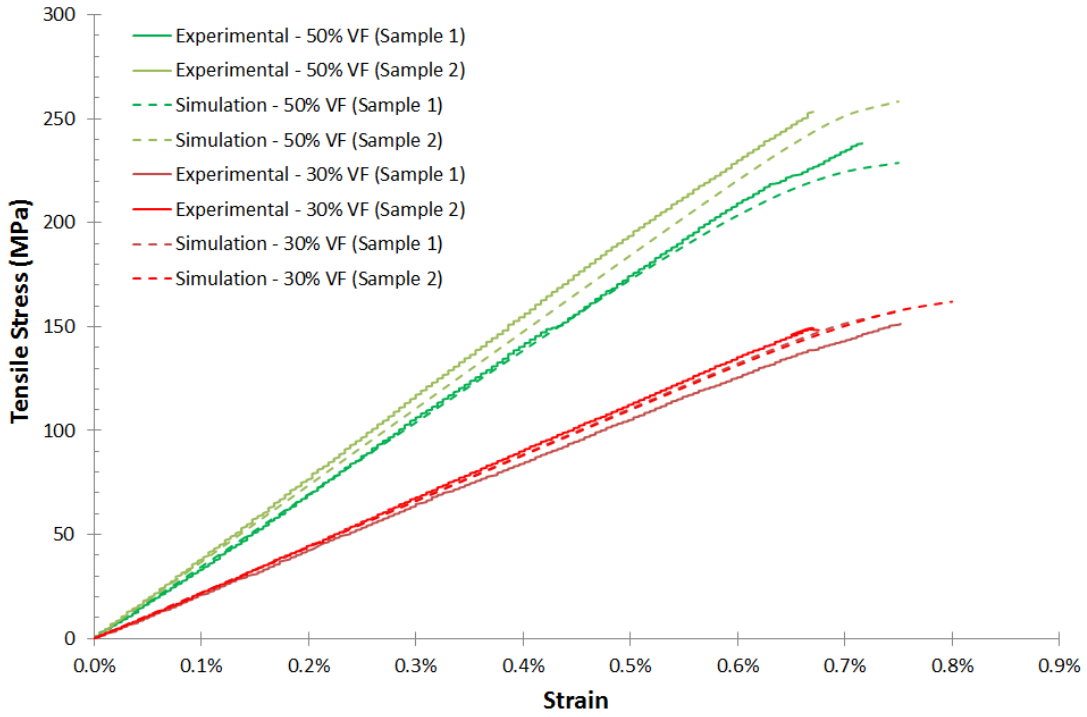

Figure 12: Comparison of typical tensile stress-strain relationships predicted using the 3D shell model against experimental data [2] for 30%Vf and 50%Vf DFCs consisting of 36mm long, 12K fibre. 12 experimental tensile tests were performed for each fibre volume fraction, but only 2 representative curves are presented.

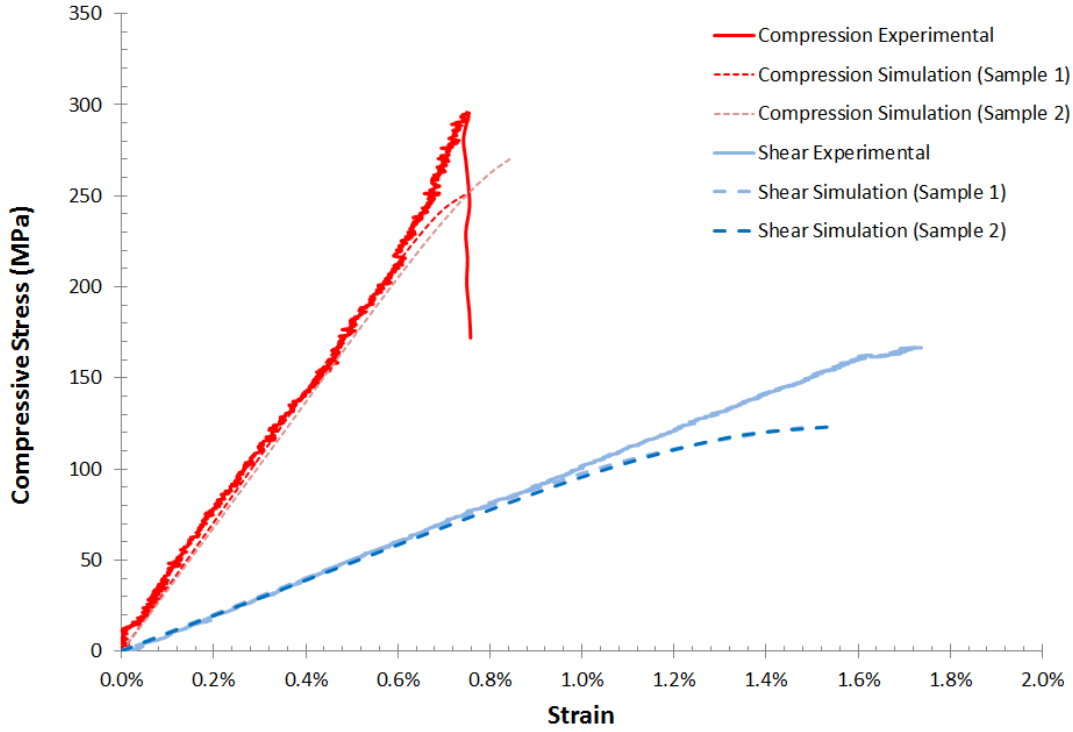

Figure 13: Comparison of typical compressive and shear stress-strain relationships predicted using the 3D shell model against experimental results in [54] for 50%Vf DFCs consisting of 36mm long, 12K fibre. Six repeats were performed for each of the experimental test types, with a representative curve presented for each.

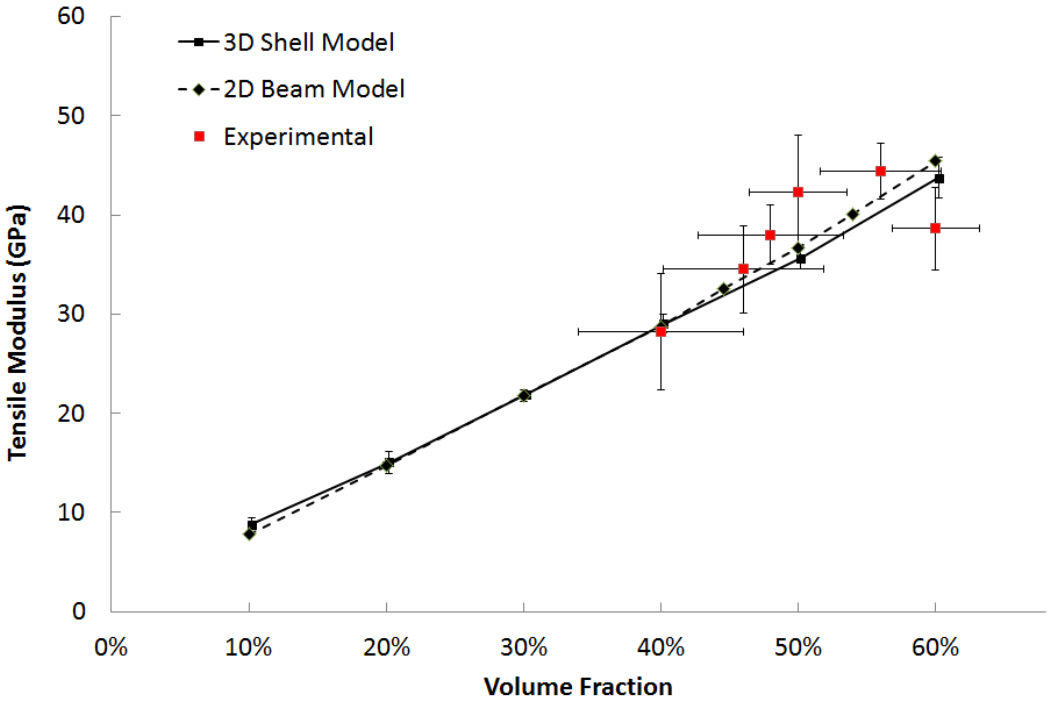

Figure 14: Comparison of tensile modulus predicted using the 3D shell model and data provided in [2]. For each fibre volume fraction, 5 repeats have been performed for 2D/3D model and 12 repeats have been performed for experimental test.

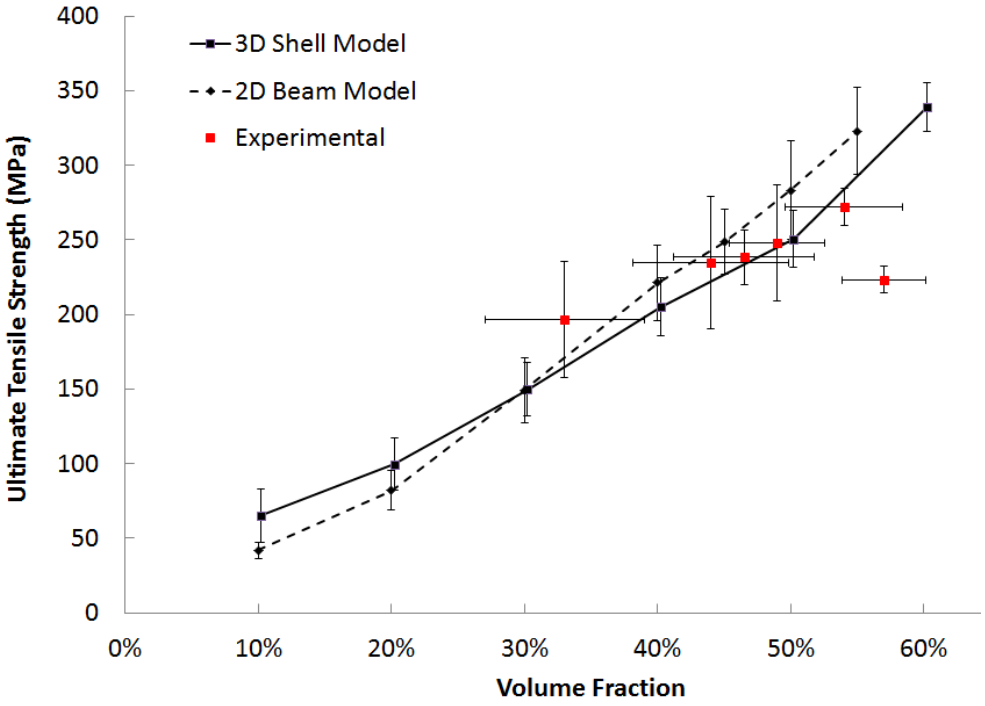

Figure 15: Comparison of tensile strength predicted using the 3D shell model and data provided in [2]. For each fibre volume fraction, 5 repeats have been performed for 2D/3D model and 12 repeats have been performed for experimental test.

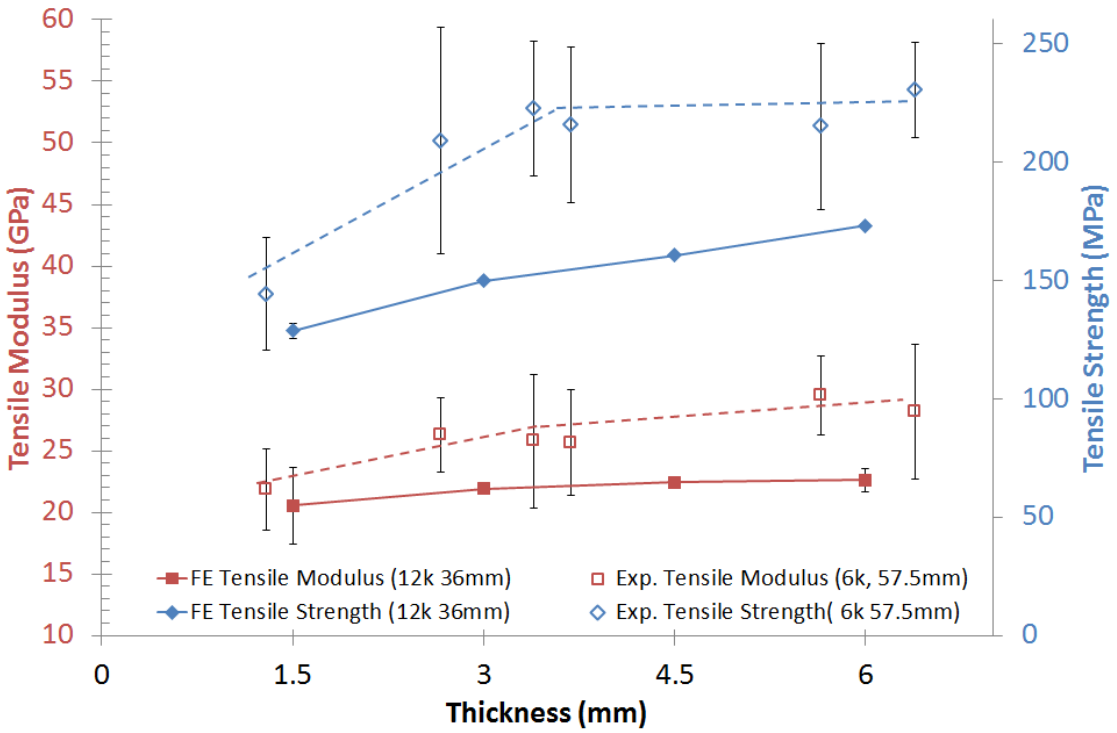

Figure 16: Tensile modulus and strength predictions as a function of coupon thickness. All FE models consist of 36mm long 12K fibres and all experimental samples consist of 57.5mm long 6K fibres [14].